2-15-2003

SPECT Imaging of Pulmonary Blood Flow in a Rat

Christian Wieholt
University of Chicago

Robert C. Molthen
Marquette University, robert.molthen@marquette.edu

Roger H. Johnson
Marquette University

Christopher A. Dawson
Medical College of Wisconsin

Anne V. Clough
Marquette University, anne.clough@marquette.edu

Published version. Published as part of the proceedings of the conference, *SPIE 5031, Medical Imaging 2003: Physiology and Function: Methods, Systems, and Applications*, 2003: 252-261. DOI.

SPECT Imaging of Pulmonary Blood Flow in a Rat

Christian Wietholt[a], Robert C. Molthen[a,b], Roger H. Johnson[a], Christopher A. Dawson[a,b] and Anne V. Clough[a]

[a]Marquette University, Milwaukee, U.S.A
[b]Medical College of Wisconsin, Milwaukee, U.S.A

ABSTRACT

Small animal imaging is experiencing rapid development due to its importance in providing high-throughput phenotypic data for functional genomics studies. We have developed a single photon emission computed tomography (SPECT) system to image the pulmonary perfusion distribution in the rat. A standard gamma camera, equipped with a pinhole collimator, was used to acquire SPECT projection images at 40 sec/view of the rat thorax following injection of Tc99m labeled albumin that accumulated in the rat's lungs. A voxel-driven, ordered-subset expectation maximization reconstruction was implemented. Following SPECT imaging, the rat was imaged using micro-CT with Feldkamp conebeam reconstruction. The two reconstructed image volumes were fused to provide a structure/function image of the rat thorax. Reconstruction accuracy and performance were evaluated using numerical simulations and actual imaging of an experimental phantom consisting of Tc99m filled chambers with known diameters and count rates. Full-width half-maximum diameter measurement errors decreased with increasing chamber diameter, ranging from $< 6\%$ down to 0.1%. Errors in the ratio of count rate estimates between tubes were also diameter dependent but still relatively small. This preliminary study suggests that SPECT will be useful for imaging and quantifying the pulmonary blood flow distribution and the distribution of Tc99m labeled ligands in the lungs of small laboratory animals.

Keywords: small animal SPECT, lung perfusion, micro-CT, image fusion, rat

1. INTRODUCTION

Small animal imaging is experiencing rapid development as a means for investigating the underlying mechanisms of disease using small animal models of human diseases and for providing phenotypic data for functional genomics. Other methods generally involve large numbers of animals sacrificed at various time points to acquire sufficient data for analysis. However, functional imaging approaches to monitoring physiological and pathophysiological processes allow acquisition of quantitative trait data in a noninvasive manner, thereby enabling longitudinal studies in the same animal. Thus, small animal imaging provides the opportunity for studying these processes in vivo and can provide three-dimensional representations of the structure or distribution of interest.

The problem of understanding structure-function relationships in the lung and how these relationships are affected by physiological adaptation in the presence of lung injury and disease has been addressed with a variety of imaging technologies[1,2,3,4,5,6,7]. To this end, we have previously reported on a microfocal x-ray system (micro-CT) developed in our laboratory to examine various aspects of pulmonary structure-function relationships including vascular and airway architecture and mechanics[9,10,11,12,13]. In the current study, we describe a single photon emission computed tomography (SPECT) system that has been developed in our laboratory to image and quantify the pulmonary perfusion distribution in the rat.

SPECT imaging of small animals requires a system that includes some form of magnification to obtain subordan level resolution. This has generally been addressed by using a pinhole geometry[14,15,16,17]. To increase sensitivity and decrease acquisition times, multi-detector[18,19,20,21] and multi-pinhole[22,23] SPECT systems have been

Further author information: (Send correspondence to A.V.C.)
A.V.C.: E-mail: anne.clough@marquette.edu, Telephone: +1 414 384 2000 x41440, Address: Research Service 151 Zablocki V.A. Medical Center, 5000 W. National Ave., Milwaukee, WI 53295-1000, U.S.A.
C.W.: E-mail: christian.wietholt@marquette.edu, Telephone: +1 414 384 2000 x41446, Address: Research Service 151 Zablocki V.A. Medical Center, 5000 W. National Ave., Milwaukee, WI 53295-1000, U.S.A.

Medical Imaging 2003: Physiology and Function: Methods, Systems, and Applications, Anne V. Clough, Amir A. Amini, Editors, Proceedings of SPIE Vol. 5031 (2003) © 2003 SPIE · 1605-7422/03/$15.00

developed. To take full advantage of the limited count rate, statistical optimization reconstruction algorithms (maximum likelihood expectation maximization (ML-EM)[24,25,26] and ordered subset expectation maximization (OS-EM)[27]) have been used, as opposed to more traditional filtered-backprojection methods[28]. ML-EM and OS-EM have been implemented using either a voxel-driven[29] or a ray-driven[30] approach, where the former has the advantage of being less complex to implement and the latter, the ability to incorporate attenuation corrections or other apriori information. These reconstruction algorithms have been used for example, in imaging of regional myocardial perfusion in the mouse[31,32]. However, to date, to the best of our knowledge, SPECT imaging of pulmonary blood flow in small animals such as mouse or rat has not been reported. Thus, we have designed and implemented a SPECT system using a standard gamma camera, a pinhole collimator, and an OS-EM reconstruction algorithm that can be used in conjunction with the micro-CT system to image pulmonary blood flow in small animals using Tc99m-labeled albumin.

2. METHODS

2.1. Imaging Systems

A Picker DYNA^{TM} MO gamma camera was used to acquire SPECT data. The camera has a sodium iodide scintillation crystal with a diameter of 260 mm. The head was equipped with a pinhole collimator with a 5mm diameter aperture. Count data acquisition and digitization was carried out with a Siemens MicroDELTA acquisition station connected over a high-speed bus system to a Digital MicroVAX 3300. The camera head was positioned in front of a precision controlled rotating specimen stage (New England Affiliated Technologies). The micro-CT system consists of a Feinfocus FXE/FXT 100.20 microfocal x-ray source (with an effective focal spot of 3μm) and a detection system consisting of an image-intensifier (Thomson TH9438 HX H661 VR24) optically coupled to a CCD camera (Silicon Mountain Design SMD1M-15) as described previously[8,9,33]. This equipment is mounted on a precision rail allowing variable magnification by altering the distances between the stage, the image intensifier, and the x-ray source. Position information is provided by linear encoders (Mitutoyo) with an accuracy of 10μm.

2.2. Imaging Methods

For SPECT data acquisition, the mobile gamma camera was positioned in front of the specimen stage and perpendicular to the x-ray beam. The center of the pinhole collimator was positioned at the height of the x-ray source for subsequent image registration purposes. The SPECT data were acquired in a step-and-shoot fashion using 128 equiangular increments over a full 360°. It was acquired with 128 x 128 pixel resolution and 16 bits per pixel grayscale resolution. Subsequently, micro-CT images were obtained by rotating the specimen in 1° increments over a full 360°. The micro-CT data were acquired with 512 x 512 pixel resolution and 8 bits per pixel grayscale resolution and transferred from the CCD camera to a frame grabber board (Imaging Technologies IM-PCI) using a RS-422 digital interface. Seven frames were acquired and averaged at each position.

2.3. Reconstruction

The SPECT data set was reconstructed using either ML-EM or its derivate, OS-EM. The reconstruction algorithm was a voxel-driven[29] implementation that incorporated decay correction using an exponential weighting function, the pinhole geometry, an interactive center-of-rotation correction, and the geometric response of a finite-sized pinhole using an inverse cone implementation[30]. The micro-CT data was reconstructed using a previously described Feldkamp conebeam reconstruction algorithm[8].

2.4. Phantom Study

An experimental phantom consisting of three test tubes embedded within a larger cylinder (diam=45mm) was constructed. Two tubes of the same diameter (diam=14mm) were each filled with 0.4mCi of technetium (Tc99m), while the smaller tube (diam=9mm) was filled with 0.2mCi. The phantom was placed on the specimen stage and imaged with a 20 sec per view acquisition time. Upon completion of all acquisitions the phantom was imaged a second time at 40 sec/view. A representative projection image obtained at 40 sec/view is shown in figure 1(a). Finally, after the SPECT acquisitions were completed, the phantom was imaged using micro-CT.

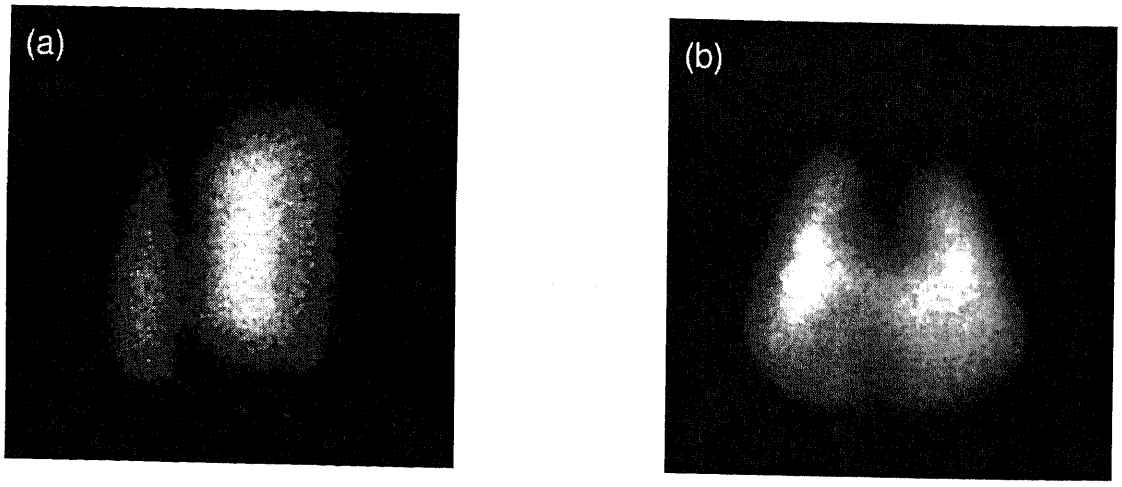

Figure 1. (a) Typical projection image of the experimental phantom. Left side of image shows projection of small tube while right side shows superposition of the two larger tubes at this view. (b) Typical projection image of the the rat lung filled with Tc99m labeled albumin, where the left and right lungs are visible.

2.5. Rat Perfusion Study

A rat was anesthetized with 40mg per kg pentobarbital sodium. A femoral venous catheter was used to inject 0.6 ml of Tc99m labeled macroaggregated albumin (MAA, Syncor International Corporation) with a total radioactivity of 2.0 mCi. After allowing the compound enough time to distribute and accumulate in the rat's lungs (approximately 2 minutes), the animal was sacrificed using an overdose of the anesthetic. The rat was then placed head down in a plastic tube (diam=52mm), and was positioned on the specimen stage. The gamma camera, equipped with the pinhole collimator, was positioned in front of the rat's thorax, where the distance between the rat and the pinhole was about 5mm. The center of rotation was set so that the right and left lungs were within the field of view at all angular positions. A set of 128 projection images was acquired in a step-and-shoot fashion with an acquisition time of 40 sec/view. A typical projection image is shown in figure 1(b) where the right and the left lungs are clearly visible.

3. SIMULATIONS

3.1. Simulation Methods

The ML-EM and the OS-EM reconstruction software was tested for accuracy and performance using computer simulations. A computer-generated activity distribution was created by simulating two large and one small cylinders within a cube in object space. The positions and intensities of the cylinders were chosen to simulate the parameters of experimental studies. One transaxial slice through the activity distribution is shown in figure 2(a).

Image data were then simulated using a forward-projector as implemented in the reconstruction software. This tool allows the user to specify the pinhole geometry of the system by providing information about the detector size, pinhole to detector distance, pinhole to object distance, pinhole diameter, and the digitization grids for the detector and object spaces. This yields a set of simulated projection images free of statistical fluctuations in count rate and spatial distribution. Subsequently, Poisson fluctuations modeling the radioactivity emission process, with a mean and variance equivalent to that observed in the experiments were created for each individual detector element. This fluctuation image was then multiplied by the corresponding simulated projection image to produce the final simulated noisy projection image. This procedure was repeated for each of the 128 angular increments. Here the GNU Scientific Library (GSL) was used to generate the Poisson fluctuations having a total of 27 million counts in the simulated acquisition. One typical simulated projection image of the activity distribution is shown in figure 2(b).

3.2. Simulation Results

The simulated projection images were reconstructed using both ML-EM and OS-EM. The root mean square (RMS) error between the original and the reconstructed activity distributions for both ML-EM and OS-EM was computed after each iteration and is shown in figure 3. A reconstruction with an RMS error smaller than 0.2% was deemed to have converged. This corresponds to approximately seventy iterations for ML-EM and only seven iterations for OS-EM in this simulation. Figure 4(a) shows the reconstruction for the simulated projection data shown in figure 2(a) using OS-EM with seven iterations .

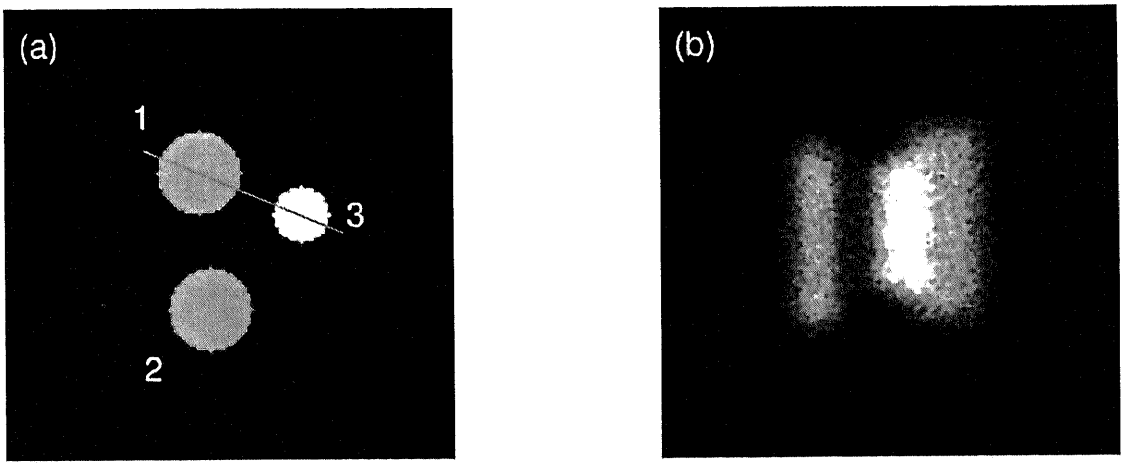

Figure 2. (a) Transaxial slice through the original computer-generated activity distribution showing the two larger tubes (1 and 2) and the smaller tube (3). The line indicates the position of the linescan shown in figure 4(b). (b) Typical simulated noisy projection image of the original activity distribution. The projection of tube 3 is seen on the left while the projection of tubes 1 and 2 are superimposed on the right.

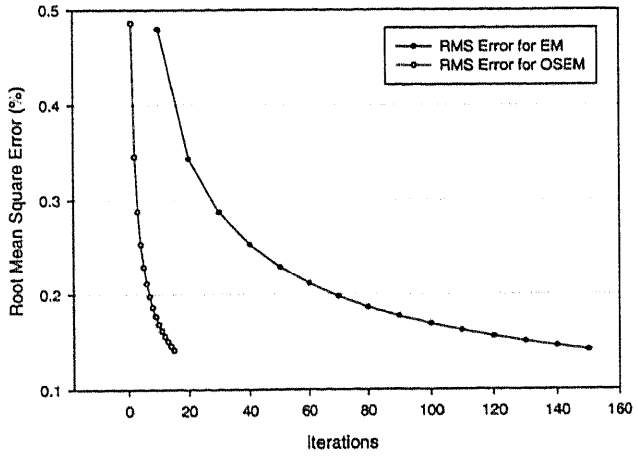

Figure 3. Root mean square (RMS) error in percent between the original and the reconstructed activity distributions after each iteration of the ML-EM or OS-EM algorithm.

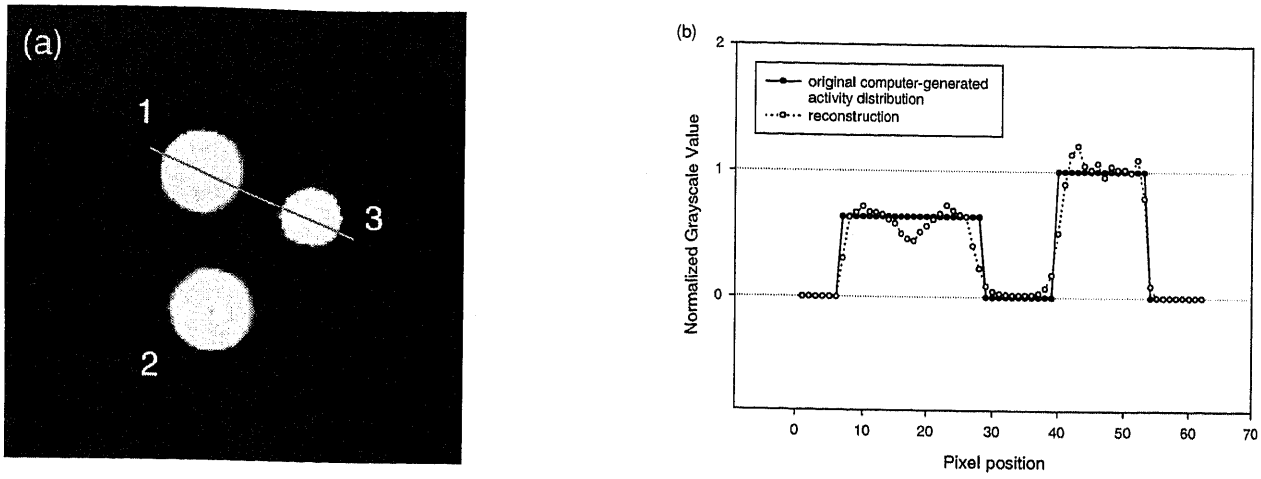

Figure 4. (a) Transaxial slice through the OS-EM reconstruction of the computer-generated activity distribution. Line indicates position of linescan shown in figure 4(b). (b) Normalized grayscale values obtained from linescans in figures 2(a) (original computer-generated activity distribution) and 4(a) (reconstructed activity distribution).

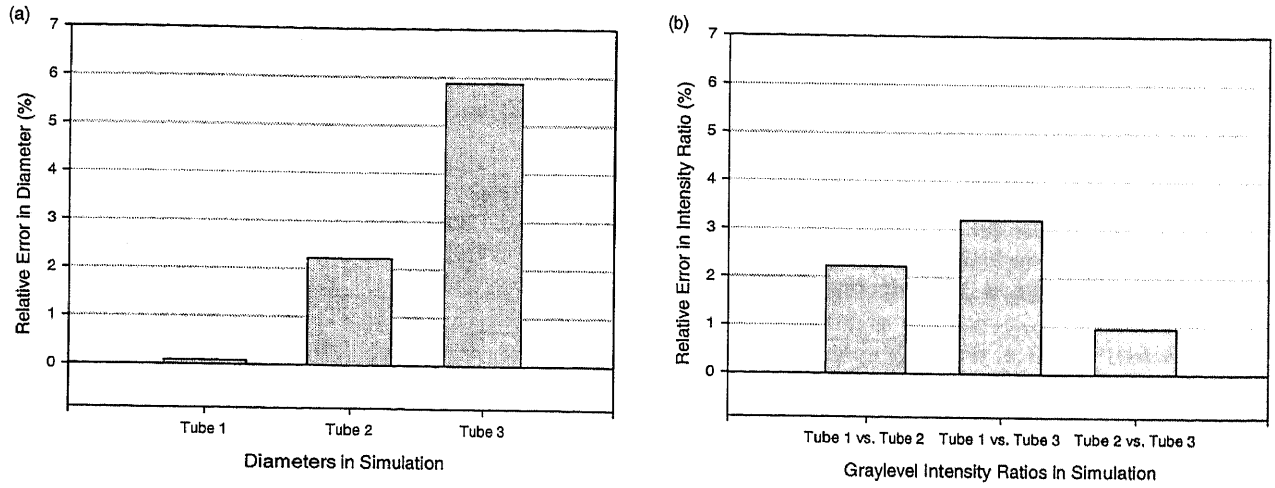

Figure 5. (a) Relative errors in tube diameter between the original and the reconstructed activity distributions. (b) Relative errors in graylevel intensity ratios for each pair of tubes between the original and the reconstructed activity distribution.

To evaluate reconstruction accuracy, full-width half-maximum (FWHM) diameter measurements were obtained from the transaxial slices using the average of six linescans, three in the horizontal and three in the vertical direction through each of the cylinders shown in figure 4(a). Linescans through the original and reconstructed activity distributions are shown in figure 4(b). The FWHM diameter measurements were compared to the true diameters and revealed a relative error that was less than $\sim$ 2% for the larger cylinders and $\sim$ 6% for the small cylinder as shown in figure 5(a).

The graylevel intensities within the reconstructed cylinders were evaluated by computing the average graylevel of a 3D ROI drawn within each cylinder. The ratio of the activity within a particular tube to that within another tube was computed for each pair of tubes using both the original and the reconstructed activity distributions. Finally, the relative error for each pair of tubes was calculated and is shown in figure 5(b). The relative error in activity for each pair was less then $\sim$ 3% in this simulation.

4. EXPERIMENTAL RESULTS

4.1. Phantom Study

The 20 sec/view and 40 sec/view tube phantom SPECT data were reconstructed using OS-EM (with seven iterations) on the original count data as well as the decay-corrected count data, to determine the relative importance of decay-correction and acquisition time. A transaxial slice trough the 40 sec/view reconstruction without decay correction is shown in figure 6(a). Reconstruction accuracy was evaluated using FWHM diameter measurements compared to the known tube diameters as described above. Figure 7(a) shows relative errors in the diameter measurements for reconstructions performed with and without decay correction. Errors for the smallest tube were around 6% while those for the larger tubes were less than 3%.

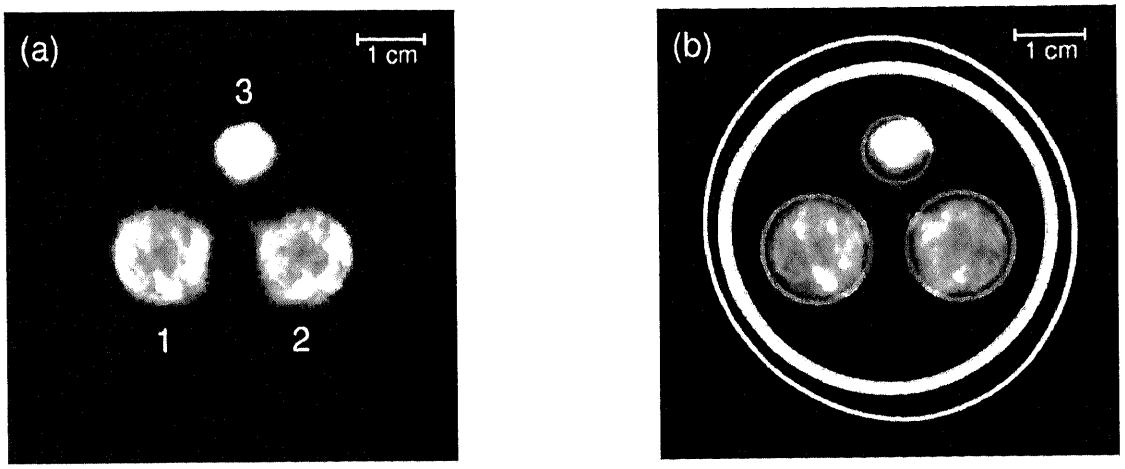

Figure 6. (a) SPECT transaxial slice through the OS-EM reconstruction of the experimental phantom using 40 sec/view projection images without decay correction. (b) Fused image of SPECT and micro-CT reconstructed transaxial slices.

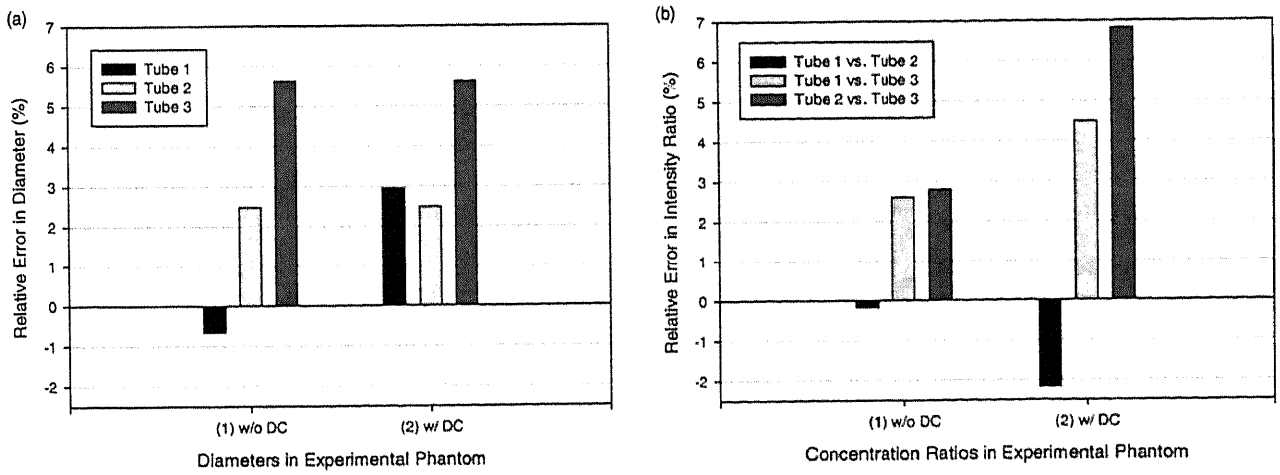

Figure 7. (a) Relative errors in diameter for the experimental phantom between the reconstructed FWHM diameter measurements and the known diameters. Projection images were reconstructed without (1) and with (2) decay correction. (b) Relative errors in concentration ratios between each pair of tubes between the reconstructed ratios and the known ratios. Projection images were reconstructed without (1) and with (2) decay correction.

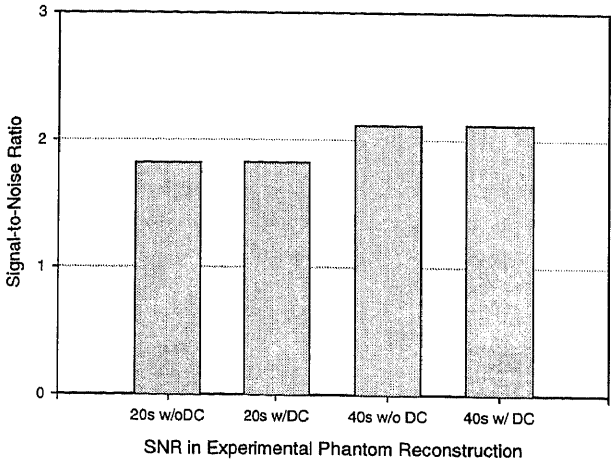

Figure 8. Estimates of signal-to-noise ratio for the experimental phantom reconstructions from acquisitions with 20 and 40 sec/view, reconstructed with (w/ DC) and without (w/o DC) decay correction.

The reconstructed estimates of graylevel intensity within each tube were evaluated using the same procedure described above for the simulations. In this case, figure 7(b) shows that the relative errors were consistently less than $\sim 7\%$ for the reconstructions with and without decay corrections for all of the pairs of tubes. In particular, when the intensities of the two tubes with the same diameter were compared, the error was $\leq 2\%$, suggesting that the larger errors in figure 7(b) are due to error in the intensity estimate from the small tube.

Signal-to-noise ratio (SNR) estimates for the 20 sec/view and 40 sec/view acquisitions were calculated for the reconstructions from a 3D ROI positioned over a large diameter tube (tube1). The SNR was computed as the ratio of the mean graylevel intensity to the standard deviation of the graylevel intensities within the ROI. Figure 8 shows no significant difference between reconstructions with- and without-decay correction, but shows $\sim 15\%$ greater SNR for the 40 sec/view over the 20 sec/view acquisition time reconstructions.

The micro-CT and the SPECT reconstruction volumes were fused using a semiautomated method. Magnification factors derived from the geometric settings for each modality, were computed to determine the voxel dimensions of each volume. The 128x128x128 SPECT volume was scaled and inverted in the x and z direction to match the 512x512x512 micro-CT volume. In this example, interactive adjustment of the angular offset, spatial positioning, and geometric size was performed. One typical resulting transaxial slice showing the resulting fused experimental phantom images is shown in figure 6(b) where the two distributions nearly superimpose.

4.2. Rat Perfusion Study

SPECT reconstructions of the rat image data were obtained using a 40 sec/view acquisitio.. ime and OS-EM. A representative transaxial slice is shown in figure 9(a). The right and left lungs are ... i sepa... in the image. The micro-CT data of the rat was reconstructed to yield a structural image in whi... ie rib ... Fusion techniques described above were applied to the reconstructed SPECT and m... -CT volumes. Figure 9(b) shows a typical transaxial slice through the fused volume where the activity with... the SPECT ima... hown to be confined to the chest as delineated by the micro-CT image.

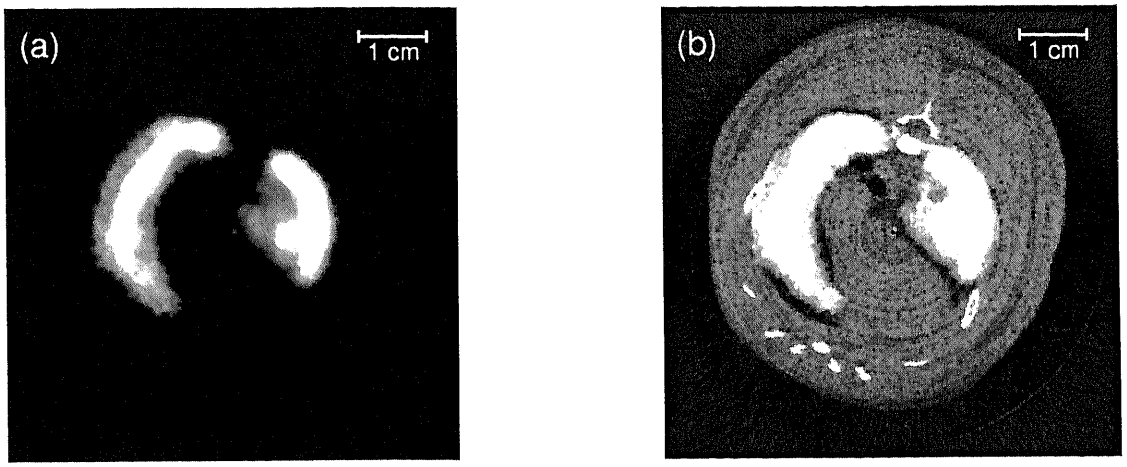

Figure 9. (a) SPECT transaxial slice through the OS-EM reconstruction of the rat lung filled with Tc99m MAA. (b) Fused image of SPECT and micro-CT reconstructed transaxial slices.

5. DISCUSSION

The simulation study and experimental phantom SPECT study were designed to evaluate the accuracy and performance of the SPECT hardware and software. These studies revealed that OS-EM converged significantly faster than ML-EM with no apparent decrease in the fidelity of the reconstructions. Also decay correction did not appear to improve the reconstructions from a resolution or SNR perspective. Finally, SNR was improved using 40 sec/view acquisition times. Thus, these options were used for the subsequent rat study.

In the current study, fusion of the anatomical micro-CT and the functional SPECT images enabled visualization of the lungs within the chest of the rat. The slight discrepancy in alignment may be attributed to subject movement between the micro-CT and SPECT acquisitions. In future work, fusion will commonly be necessary to identify the lung field for studying both hemodynamic and metabolic functions of the lung, when, unlike the Tc99m MAA, the radiolabeled compounds of interest are distributed to other tissues in addition to the lungs (e.g., heart, chest wall and close sub-diaphragmatic organs). Thus it will be necessary to identify the lung field using CT.

The SPECT system has been designed and optimized in this study to evaluate lung perfusion in a rat. This approach will be used to perform longitudinal studies of vascular remodeling that occurs in response to exposure to chronic hypoxia in the rat and to study bronchial angiogenesis, which may be particularly important with regard to lung cancers whose blood supply is via the bronchial circulation rather than the pulmonary circulation. Further application of the SPECT system includes the possibility of evaluating the physiological or pathophysiological status of the lungs from measurements of their ability to take up and/or metabolize various radiolabeled ligands and substrates in reactions that are affected by the lung status. Kinetic modeling can then be used to quantify and separate the reactions of interest from other processes that influence the substrate disposition.

6. CONCLUSION

We have described a SPECT system designed to image pulmonary blood flow in a rat. The method was successful in visualizing pulmonary blood flow and in particular, the right and left lungs are clearly identifiable within the SPECT images. Future work will be aimed at upgrading the hardware and software of the system for improving spatial resolution in order to quantify the within-lung regional flow distribution. This includes implementation of a ray-driven OS-EM reconstruction algorithm in order to incorporate a non-uniform attenuation correction where the attenuation coefficients will be obtained from the micro-CT images. This will require further improvements in the image registration and fusion methods.

ACKNOWLEDGMENTS

This work was supported by HL 19298, NSF BES 9818197, NIH BRP HL 64368, W.M. Keck Foundation, Bagozzi Graduate Fellowship and Department of Veterans Affairs.

REFERENCES

1. E. M. F. Damen, S. H. Muller, L. J. Boersma, R. W. de Boer, and J. V. Lebesque, "Quantifying local lung perfusion and ventilation using correlated SPECT and CT data," *The Journal of Nuclear Medicine* **35**, pp. 784–792, 1994.
2. L. Ketai and M. Hartshorne, "Potential uses of computed tomography-SPECT and computed tomography-coincidence fusion images of the chest," *Clinical Nuclear Medicine* **26**, pp. 433–441, 2001.
3. J. Palmer, U. Bitzen, B. Jonson, and M. Bajc, "Comprehensive ventilation/perfusion SPECT," *Journal of Nuclear Medicine* **42**, pp. 1288–1294, 2001.
4. C. V. Heidi, C. Schwickert, H.-U. Kauczor, R. Piepenburg, F. Schweden, H. H. Schild, S. Iversen, and M. Thelen, "CT im Vergleich mit SPECT bei chronisch rezidivierender Lungenembolie: Hyperdensien als Zeichen pulmonalarterieller Hyperperfusion ?," *Fortschritte auf dem Gebiet der Roentgenstrahlen* **162**, pp. 199–203, 1995.
5. M. Bajc, U. Bitzen, B. Olsson, V. P. de Sa, J. Palmer, and B. Jonson, "Lung ventilation/perfusion SPECT in the artificially embolized pig," *Journal of Nuclear Medicine* **43**, pp. 640–647, 2002.
6. S. A. Wood, E. A. Zerhouni, J. D. Hoford, E. A. Hoffman, and W. Mitzner, "Measurement of three-dimensional lung tree structures by using computed tomography," *Journal of Applied Physiology* **79**, pp. 1687–1697, 1995.
7. E. A. Hoffman and G. McLennan, "Assessment of the pulmonary structure-function relationship and clinical outcomes measures : qualitative volumetric CT of the lung," *Academic Radiology* **4**, pp. 758–776, 1997.
8. R. H. Johnson, H. Hu, S. T. Haworth, P. S. Cho, C. A. Dawson, and J. H. Linehan, "Feldkamp and circle-and-line cone-beam reconstruction for 3D micro-CT of vascular networks," *Physics in Medicine and Biology* **43**, pp. 929–940, 1998.
9. R. C. Molthen, C. Wietholt, S. T. Haworth, and C. A. Dawson, "Estimation of pulmonary arterial volume changes in the normal and hypertensive fawn-hooded rat from 3D Micor-CT data," in *SPIE Medical Imaging 2002 Physiology and Function from Multidimensional Images*, A. V. Clough and C.-T. Chen, eds., *Proc. SPIE* **4683**, pp. 266–275, 2002.
10. A. V. Clough, S. T. Haworth, W. Ma, and C. A. Dawson, "Effects of hypoxia on pulmonary microvascular volume," *Am. J. Physiol. Heart Circ. Physiol.* **279**, pp. H1274–H1282, 2000.
11. A. Al-Tinawi, G. S. Krenz, D. A. Rickaby, J. H. Linehan, and C. A. Dawson, "Influence of hypoxia and serotonin on small pulmonary vessels," *J. Appl. Physiol.* **76**, pp. 56–65, 1994.
12. K. L. Karau, R. H. Johnson, R. C. Molthen, A. H. Dhyani, S. T. Haworth, C. C. Hanger, D. L. Roerig, and C. A. Dawson, "Microfocal X-ray CT imaging and pulmonary arterial distensibility in excised rat lungs.," *Am. J. Physiol. Heart Circ.* **281**, pp. H1447–H1457, 2001.
13. R. H. Johnson, R. C. Molthen, K. L. Karau, C. C. Hanger, S. T. Haworth, C. A. Dawson, and J. H. Linehan, "Analysis of 3D pulmonary microangiograms," in *Computer-aided Diagnosis in Medical Imaging*, K. Doi, H. MacMahon, M. Giger, and K. Hoffmann, eds., *Excerpta Medica International Congress Series* **1182**, pp. 369–376, (Amsterdam), 1999.
14. D. A. Weber and M. Ivanovic, "Pinhole SPECT: Ultra-high resolution imaging for small animal studies," *Journal of Nuclear Medicine* **36**, pp. 2287–2289, 1995.
15. K. Ogawa, T. Kawade, K. Nakamura, A. Kubo, and T. Ichihara, "Ultra high resolution pinhole SPECT for small animal study," *IEEE Transactions on Nuclear Science* **45**, pp. 3122–3126, 1998.
16. L. R. MacDonald, B. E. Patt, J. S. Iwanczyk, B. M. W. Tsui, Y. Wang, E. C. Frey, D. E. Wessell, P. D. Acton, and H. F. Kung, "Pinhole SPECT of mice using the LumaGEM gamma camera," *IEEE Transactions on Nuclear Science* **48**, pp. 830–836, 2001.

17. B. H. Hasegawa, K. Iwata, K. H. Wong, M. C. Wu, A. D. Silva, H. R. Tang, W. C. Barber, A. B. Hwang, and A. E. Sakdinawat, "Dual-modality imaging of function and physiology," in *SPIE Medical Imaging 2002 Physiology and Function from Multidimensional Images*, A. V. Clough and C.-T. Chen, eds., *Proc. SPIE* **4683**, pp. 1–15, 2002.
18. K. Ishizu, T. Mukai, Y. Yonekura, M. Pagani, T. Fujita, Y. Magata, S. Nishizawa, N. Tamaki, H.Shibasaki, and J. Konishi, "Ultra-high resolution SPECT system using four pinhole collimators for small animal studies," *Journal of Nuclear Medicine* **36**, pp. 2282–2287, 1995.
19. W. P. Klein, H. H. Barrett, I. W. Pang, D. D. Patton, M. M. Rogulski, J. D. Sain, and W. E. Smith, "FASTSPECT: Electrical and mechanical design of a high-resolution dynamic SPECT imager," in *Conference Record of the 1995 IEEE Nuclear Science Symposium and Medical Imaging, San Franscisco*, **2**, pp. 931–933, IEEE, 1995.
20. D. W. Wilson, H. H. Barrett, and L. R. Furenlid, "A new design for a SPECT small-animal imager," *Nuclear Science Symposium Conference Record* **3**, pp. 1826–1829, 2002.
21. B. M. W. Tsui, Y. C. Wang, E. C. Frey, and D. E. Wessell, "High resolution pinhole SPECT imaging of small animals using scintillation camera," in *High Resolution Imaging in Small Animals: Instrumentation, Applications and Animal Handling*, pp. 145–147, Sep. 2001.
22. D. Schellingerhout, R. Accorsi, U. Mahmood, R. Weissleder, and R. C. Lanza, "High-resolution coded aperture planar scintigraphy of small animals," in *High Resolution Imaging in Small Animals: Instrumentation, Applications and Animal Handling*, pp. 119–121, Sep. 2001.
23. N. U. Schramm, A. Wirrwar, H. H. Coenen, and H. Halling, "Multi-pinhole collimation for high-sensitivity SPECT imaging of small animals," in *High Resolution Imaging in Small Animals: Instrumentation, Applications and Animal Handling*, pp. 76–78, Sep. 2001.
24. L. A. Shepp and Y. Vardi, "Maximum likelihood reconstruction for emission tomography," *IEEE Transactions on Medical Imaging* **MI-1**, pp. 113–122, 1982.
25. J. Kay, "The EM algorithm in medical imaging," *Statistical Methods in Medical Research* **6**, pp. 55–75, 1997.
26. K. Lange and R. Carson, "EM reconstruction algorithms for emission and transmission tomography," *Journal of Computer Assisted Tomography* **8**, pp. 306–316, 1984.
27. H. M. Hudson and R. S. Larkin, "Accelerated image reconstruction using ordered subsets of projection data," *IEEE Transactions on Medical Imaging* **13**, pp. 601–609, 1994.
28. J. Li, R. J. Jaszczak, and K. L. G. adn R. E. Coleman, "A filtered backprojection algorithm for pinhole SPECT with a displaced centre of rotation," *Phys. Med. Biol.* **39**, pp. 165–176, 1994.
29. N. Schramm, *Entwicklung eines hochaufloesenden Einzelphotonen-Tomographen fuer kleine Objekte*. PhD thesis, Universitaet Goettingen, 2001.
30. G. L. Zeng, G. T. Gullberg, B. M. W. Tsui, and J. A. Terry, "Three-dimensional iterative reconstruction algorithms with attenuation and geometric point response correction," *IEEE Transactions on Nuclear Science* **38**, pp. 693–702, 1991.
31. M. C. Wu, H. R. Tang, D. W. Gao, A. Ido, J. W. O'Connell, B. H. Hasegawa, and M. W. Dae, "ECG-gated pinhole SPECT in mice with millimeter spatial resolution," *IEEE Transactions on Nuclear Science* **47**(3), pp. 1218–1221, 2000.
32. Z. Liu, G. A. Kastis, G. D. Stevenson, H. H. Barrett, L. R. Furenlid, M. A. Kupinski, D. D. Patton, and D. W. Wilson, "Quantitative analysis of acute myocardial infarct rat hearts with ischemia-reperfusion using a high-resolution stationary spect system," *The Journal of Nuclear Medicine* **43**, pp. 933–939, 2002.
33. R. C. Molthen, S. T. Haworth, D. Roerig, C. Hanger, R. Johnson, and C. A. Dawson, "Cone-beam x-ray micro-computed tomography with concurrent dynamic planar angiographic imaging and physiological measurement," in *High Resolution Imaging in Small Animals: Instrumentation, Applications and Animal Handling, Proc. HiRes*, pp. 253–255, 2001.